Structural Insights into Substrate Recognition and Activity Regulation of the Key Decarboxylase SbnH in Staphyloferrin B Biosynthesis

Jieyu Tang[1,2,†], Yingchen Ju[1,2,†], Qiong Gu[2], Jun Xu[2] and Huihao Zhou[1,2]

1 - Guangdong Provincial Key Laboratory of Chiral Molecule and Drug Discovery, *School of Pharmaceutical Sciences, Sun Yat-sen University, Guangzhou 510006, China*
2 - Research Center for Drug Discovery, *School of Pharmaceutical Sciences, Sun Yat-sen University, Guangzhou 510006, China*

Correspondence to Huihao Zhou: *Guangdong Provincial Key Laboratory of Chiral Molecule and Drug Discovery, School of Pharmaceutical Sciences, Sun Yat-sen University, Guangzhou 510006, China.* zhuihao@mail.sysu.edu.cn
https://doi.org/10.1016/j.jmb.2019.10.009
Edited by M. Guss

Abstract

Staphyloferrin B is a hydroxycarboxylate siderophore that is crucial for the invasion and virulence of *Staphylococcus aureus* in mammalian hosts where free iron ions are scarce. The assembly of staphyloferrin B involves four enzymatic steps, in which SbnH, a pyridoxal 5′-phosphate (PLP)-dependent decarboxylase, catalyzes the second step. Here, we report the X-ray crystal structures of *S. aureus* SbnH (*Sa*SbnH) in complex with PLP, citrate, and the decarboxylation product citryl-diaminoethane (citryl-Dae). The overall structure of *Sa*SbnH resembles those of the previously reported PLP-dependent amino acid decarboxylases, but the active site of *Sa*SbnH showed unique structural features. Structural and mutagenesis analysis revealed that the citryl moiety of the substrate citryl-L-2,3-diaminopropionic acid (citryl-L-Dap) inserts into a narrow groove at the dimer interface of *Sa*SbnH and forms hydrogen bonding interactions with both subunits. In the active site, a conserved lysine residue forms an aldimine linkage with the cofactor PLP, and a phenylalanine residue is essential for accommodating the L-configuration Dap of the substrate. Interestingly, the freestanding citrate molecule was found to bind to *Sa*SbnH in a conformation inverse to that of the citryl group of citryl-Dae and efficiently inhibit *Sa*SbnH. As an intermediate in the tricarboxylic acid (TCA) cycle, citrate is highly abundant in bacterial cells until iron depletion; thus, its inhibition of *Sa*SbnH may serve as an iron-dependent regulatory mechanism in staphyloferrin B biosynthesis.

Introduction

Iron is an essential nutrient for the growth of microorganisms. However, iron in the human body mostly exists in complexes with heme or proteins, leaving free iron scarce [1]. One of the most common strategies used by bacteria for surviving in iron-restricted environments is to secrete low molecular weight ferric-chelating compounds, named siderophores, to capture ferric ions from the environment, and after chelating iron, the siderophore-iron complexes are transferred into bacterial cells through specific receptors and transporters [2,3]. In response, mammalian hosts can produce siderophore-binding proteins to eliminate siderophores, preventing microbial growth, which is so called "nutritional immunity" [4]. Although increasing antibiotic resistance requires novel and effective antibacterial strategies, this kind of "battle" between host and bacteria suggests an interesting way to combat microbial infection by targeting siderophore-based iron uptake systems of multidrug-resistant bacteria [5,6].

Staphylococcus aureus is a notorious gram-positive pathogenic bacterium that causes diseases from skin infections to serious systemic diseases such as septic shock and pneumonia [7]. To obtain enough ferric ions from the environment in human hosts, *S. aureus* synthesizes at least two α-hydroxycarboxylate type siderophores, staphyloferrin A and B [8,9]. Staphyloferrin A is widespread among *Staphylococcus* species and more likely functions as a housekeeping iron captor conducive to commensalistic colonization, whereas staphyloferrin B is

mainly produced in pathogenic coagulase-positive staphylococci and plays more significant roles in invasive infection [10,11]. The expression level of the biosynthetic locus of staphyloferrin B, but not staphyloferrin A, is strongly upregulated in iron-depleted environments, such as in human blood, compared with that in iron-rich environments [12,13]. Knockout of the *sbn* operon or its regulator gene *sbnI* strongly restricted *S. aureus* growth in iron-restricted medium [14]. The *S. aureus* strain with a mutation in *sbnE*, the gene encoding the synthetase SbnE, which is essential for the biosynthesis of staphyloferrin B, showed a much lower colony number in comparison with its parent strain in a murine kidney abscess model of *S. aureus* infection [15], indicating that staphyloferrin B is crucial for the growth and pathogenicity of *S. aureus* within the host. Furthermore, a recent study identified that baulamycins A and B, two natural products from *Streptomyces tempisquensis*, inhibit the growth of *S. aureus in vitro*, with IC_{50} values of 4.8 μM and 19 μM, respectively, through inhibiting SbnE [16]; this result provided important chemical evidence for using the staphyloferrin B biosynthesis pathway as a new antibacterial target.

The genetic locus of staphyloferrin B in *S. aureus* encodes twelve proteins. Among those, SbnD and SirA, B, and C are responsible for the export and import of staphyloferrin B across the *S. aureus* membrane. SbnA, B, G, and I are responsible for preparing staphyloferrin B building blocks such as citrate, L-2,3-diaminopropionic acid (L-Dap) and α-ketoglutarate (α-KG). These building blocks are then used by three nonribosomal peptide synthetase-independent siderophore (NIS) synthetases SbnC, E, F and a decarboxylase SbnH to assemble staphyloferrin B. During the assembly process, SbnE first links an L-Dap to citrate, and SbnH decarboxylates the intermediate product before it can be further used as the substrate by SbnC and F, finishing staphyloferrin B biosynthesis (Supplementary Fig. S1) [17]. SbnH is a group IV pyridoxal 5′-phosphate (PLP)-dependent decarboxylase, which is widely found in the metabolism of nitrogen-containing small molecules such as lysine, ornithine, and arginine [18]. These decarboxylases all contain a conserved lysine residue to covalently bind with PLP by forming a lysine-PLP aldimine. When decarboxylation occurs, PLP changes to form an external aldimine with the amino group of the substrate, and then the carboxyl group is cleaved [19]. Notably, many of these PLP-dependent decarboxylases are considered drug targets. For the ornithine decarboxylase (ODC) in polyamine synthesis, its ornithine-mimic covalent inhibitor α-difluoromethylornithine (DFMO) has been clinically used in the treatment of African trypanosomiasis for nearly 30 years [20,21] and was further approved by FDA to treat hirsutism since 2000 [22]. More recently, the potential of using human ODC as a target for treating Alzheimer's disease has also been discussed [23,24]. In addition, the bacterial diaminopimelate decarboxylase (DAPDC), an essential enzyme involved in both diaminopimelate metabolism and lysine biosynthesis, is a promising target for antibiotic discovery [25]. Although SbnH shares significant similarity with ODC and DAPDC, the active pocket of SbnH might also be druggable. However, more structural and mechanistic details are required for the discovery of SbnH inhibitors.

In this study, we provide the first structural study of SbnH from *S. aureus* (*Sa*SbnH). The cofactor and substrate-binding mechanisms of *Sa*SbnH were revealed by cocrystal structures and site-directed mutagenesis analysis. The citrate molecule was observed to bind to *Sa*SbnH with an unexpected conformation and efficiently inhibit the catalytic activity of *Sa*SbnH, and the structural mechanism and the possible biological significance of *Sa*SbnH-citrate interactions were also discussed.

Results

The overall structure of *Sa*SbnH

*Sa*SbnH belongs to the group IV PLP-dependent decarboxylase family, and the overall structure of *Sa*SbnH resembles these family members [18]. The structure of *Sa*SbnH consists of two domains (Fig. 1a). Residues 25–275 form an atypical eight-fold α/β-barrel. In contrast to the barrel structure of triosephosphate isomerase (TIM), the α/β-barrel of *Sa*SbnH starts with an α-helix, not a β-strand. The N-terminal sequence (res. 1–24) forms an α-helix and a β-strand and folds together with the C-terminal part of *Sa*SbnH (res. 310–374) to form a mostly β-sandwich structure.

Searching using DALI [26] revealed that the closest structural homologs of *Sa*SbnH in PDB are mainly amino acid decarboxylases, including DAPDC, ODC, lysine decarboxylase (LDC), and arginine decarboxylase (ADC) (Supplementary Table S1) [27–30]. Structural superimposition revealed that most of the structural differences in *Sa*SbnH and its homologs were present in their β-sandwich domains (Fig. 1b). For example, residues Arg319 to Val330 in *Sa*SbnH form a significantly longer loop than other homologous decarboxylases (Fig. 1b and Supplementary Fig. S2) and contribute additional hydrogen bonding interactions and hydrophobic stacks with the α/β-barrel domain of another *Sa*SbnH molecule.

An asymmetric unit of the *Sa*SbnH crystal contains three *Sa*SbnH monomers, and two of them form a symmetric homodimer with an interface of 2930 $Å^2$ as calculated by PDBePISA [31]. The third monomer

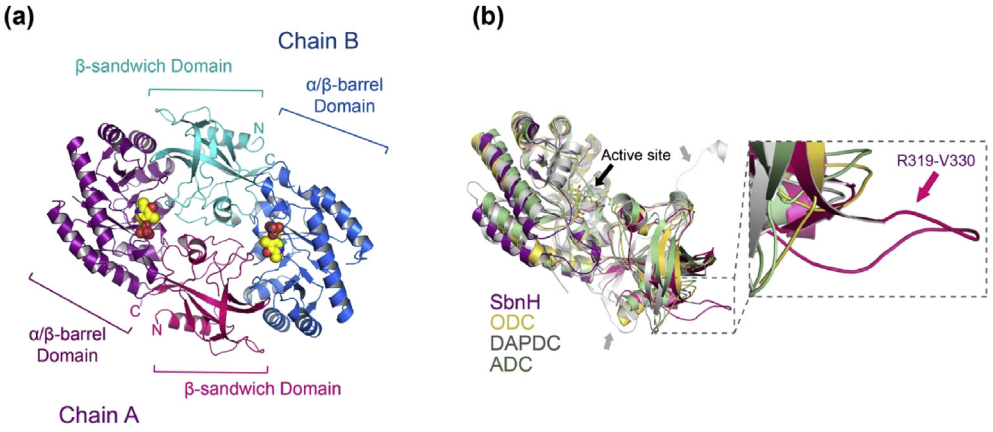

Fig. 1. The overall structure of *Sa*SbnH. (a) A homodimer of *Sa*SbnH is presented as a cartoon, and the cofactor PLP is shown as spheres in the two active sites. Two *Sa*SbnH monomers are colored purple (chain A) and blue (chain B), and each *Sa*SbnH monomer can be divided into two domains: α/β-barrel domain (dark color) and β-sandwich domain (light color). For PLP, the carbon atoms are colored yellow; the nitrogen atoms, blue; and oxygen atoms, red. (b) Superposition of a *Sa*SbnH monomer with its homologs *Vibrio vulnificus* ODC (PDB ID: 2PLJ, yellow), *Methanocaldococcus jannaschii* DAPDC (PDB ID: 1TWI, white), and *Paramecium bursaria* Chlorella virus 1 ADC (PDB ID: 2NVA, green). *Sa*SbnH is colored the same as chain A in (a). The obvious differences between *Sa*SbnH and its homologs are mainly observed at their β-sandwich domains, and a significant longer loop in SbnH and additional structures at N- and C-terminus of DAPDC are indicated by arrows.

forms a similar dimer with another *Sa*SbnH monomer from the adjacent asymmetric unit. The gel filtration experiments confirmed that *Sa*SbnH also forms dimers in solution, similar to other group IV PLP-dependent decarboxylases (Supplementary Fig. S3) [32]. Although PLP was not supplemented during protein purification and crystallization, PLP (one per *Sa*SbnH monomer) was observed to be bound to the C-terminal end of the α/β-barrel and formed an aldimine linkage with residue Lys50 on the loop behind the first β-strand of the α/β-barrel (Fig. 1a, and Supplementary Fig. S4). Other residues and hydrogen bonding interactions for coordinating and orientating the 5′-phosphate group and the pyridine nitrogen of PLP are conserved to other PLP-dependent amino acid decarboxylases (Supplementary Figs. S2 and S4) [33].

Substrate recognition by *Sa*SbnH

To understand how *Sa*SbnH recognizes its substrate citryl-L-Dap, crystals of the *Sa*SbnH_K50A variant were soaked with a reaction mixture containing the biosynthesized citryl-L-Dap (see Methods and Materials). Although the conserved lysine residue was proposed to play important roles in PLP binding and catalysis [34], the electron density of the *Sa*SbnH_K50A crystal indicated that the decarboxylated product citryl-Dae was bound in the active sites of two of the three *Sa*SbnH molecules in the asymmetric unit (Fig. 2a and b). The enzymatic assay also showed that the *Sa*SbnH_K50A variant retains weak but detectable activity (less than 10% in comparison with wild-type *Sa*SbnH; see below for details). One citryl-Dae molecule was in a PLP-coupled form, and the other was freestanding with its Dae moiety exposed to the solvent. At the active site of the third *Sa*SbnH monomer, the density was too weak to unambiguously model a ligand. The complex structure with citryl-Dae indicated that the substrate-binding pocket of *Sa*SbnH consists of a narrow groove between the C-terminal β-sandwich domains of two *Sa*SbnH monomers of the dimer (Supplementary Fig. S5).

The citryl-Dae molecule binds to the substrate-binding groove mainly through extensive hydrophilic interactions between its citryl moiety and the residues from both *Sa*SbnH monomers (Fig. 2a and b). The oxygen of the amido bond forms two hydrogen bonds with Arg269, the remaining prochiral carboxyl group forms a hydrogen bond with Ser308 and salt bridge interactions with Arg304, and the central carboxyl group forms a hydrogen bond with Trp309 and another hydrogen bond with Thr345 from the other *Sa*SbnH monomer of the dimer. Furthermore, the side chain of Lys347 stretches across the citryl moiety and helps to lock the citryl moiety into the substrate-binding groove (Fig. 2a and b). Most citryl-binding residues could be well superimposed between the citryl-Dae-bound and unbound structures, and only Arg269 and Trp309 shifted slightly towards the citryl moiety upon citryl-Dae binding (Fig. 2c). These citryl-binding residues were analyzed by site-directed mutagenesis, and all the mutations, except S308A, strongly impaired the activity of *Sa*SbnH, supporting their important roles

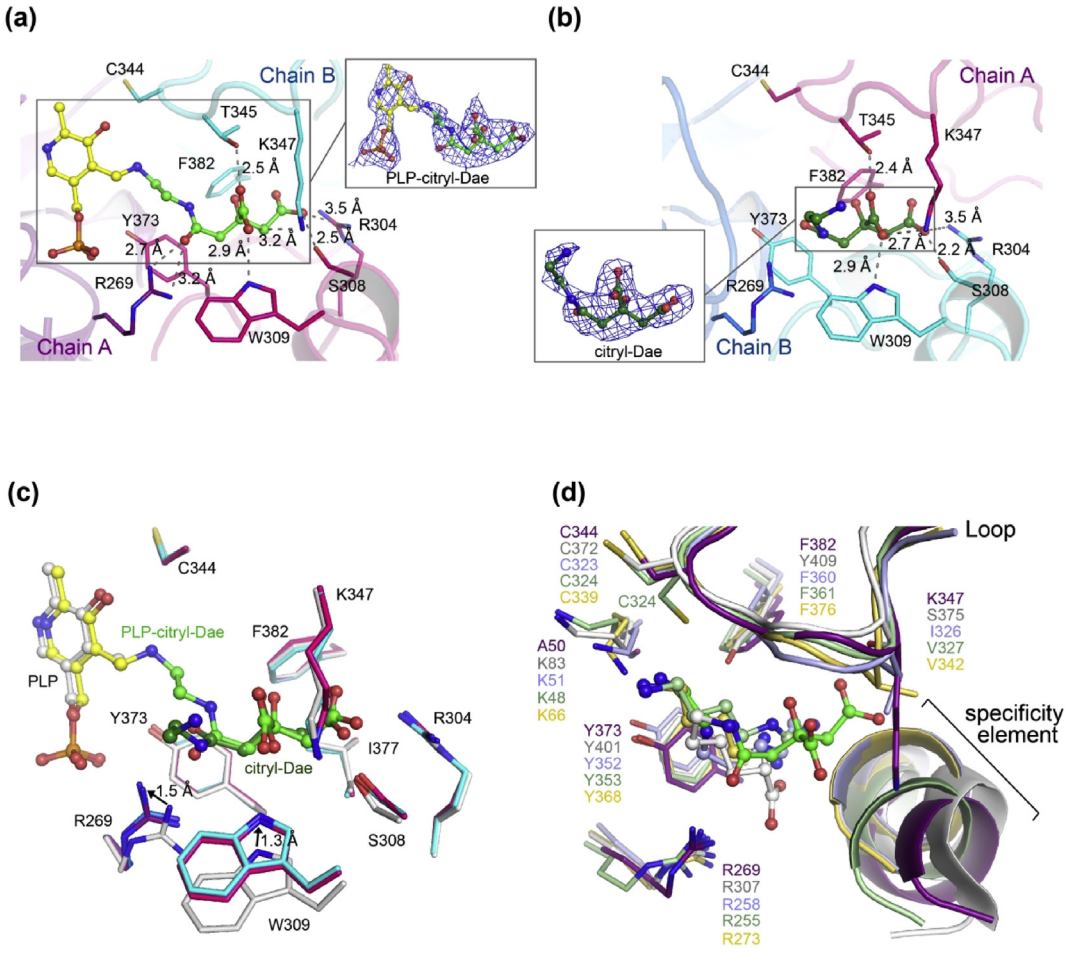

Fig. 2. Substrate recognition by *Sa*SbnH. (a, b) The PLP-coupled citryl-Dae and freestanding citryl-Dae are shown as sticks in the two active sites of the *Sa*SbnH dimer. PLP is colored the same as in Fig. 1a, and citryl-Dae is colored green. Two *Sa*SbnH monomers are shown as cartoons and colored the same as in Fig. 1a, and the key residues involved in the recognition of citryl-Dae are shown as sticks. Citryl-Dae forms multiple hydrogen bonds with *Sa*SbnH, which are drawn as gray dashed lines. The $2F_o-F_c$ composite maps around PLP-citryl-Dae and citryl-Dae are contoured at 1.0 σ and shown as blue mesh. (c) Superposition of the active site of *Sa*SbnH bound or unbound with citryl-Dae. The compound and the substrate-binding residues of *Sa*SbnH are drawn as sticks. The apo state is colored white, and the PLP-citryl-Dae bound state and citryl-Dae bound state are colored the same as in Fig. 2a and b, respectively. Only the side chains of Arg209 and Trp309 shifted a few angstroms upon substrate binding. (d) Structural comparison of the substrate-binding pocket of *Sa*SbnH (purple) with its homologs *Vibrio vulnificus* ODC (PDB ID: 2PLJ, yellow), *Methanocaldococcus jannaschii* DAPDC (PDB ID: 1TWI, white), *Paramecium bursaria* Chlorella virus 1 ADC (PDB ID: 2NVA, green), and *Selenomonas ruminantium* LDC (PDB ID: 5GJM, light blue). The distance between the "specificity helix" and PLP is variable among these amino acid decarboxylases to accommodate substrates of different sizes. In *Sa*SbnH, the citryl-Dae inserts its citryl group into the narrow groove between the specificity helix and a loop from the two *Sa*SbnH monomers of the homodimer.

in substrate binding (Fig. 3). Considering the similar side chain size between serine and alanine, the S308A mutation might only disrupt a hydrogen bond but not change the shape of the substrate-binding groove. Thus, it is reasonable that the S308A mutation did not significantly impair the decarboxylation of citryl-L-Dap like other mutations.

Previous structural studies found that the active sites of almost all of the homologous amino acid decarboxylases are remarkably similar to each other except for the position of the "specificity element," a short 3_{10}-helix at the back of substrate-binding pocket (Fig. 2d). The distance between the 3_{10}-helix and PLP determines the size of the amino acid substrates that can be accommodated [28]. Interestingly, the specificity element of *Sa*SbnH did not shift further to accommodate citryl-Dae, a compound larger than the amino acid substrates. Instead, the citryl moiety of citryl-Dae turned to another direction and inserted into the narrow groove between the

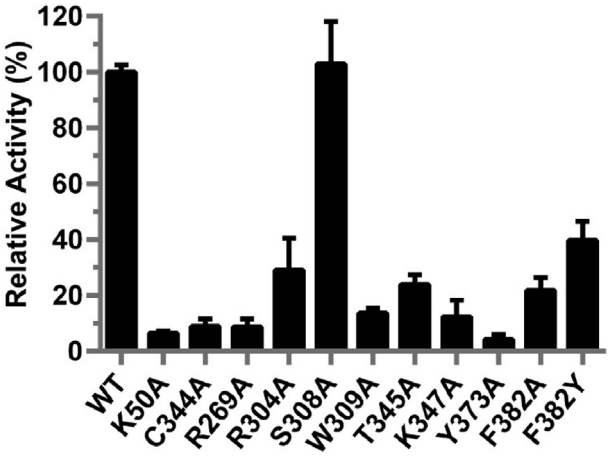

Fig. 3. The catalytic activities of *Sa*SbnH and its variants. The residues involved in substrate binding and catalysis were mutated. The ATP consumption of the reactions containing each *Sa*SbnH variant was measured and compared with wild-type *Sa*SbnH.

specificity element and a loop from another *Sa*SbnH monomer of the homodimer. In addition, the specificity element 3_{10}-helix is a standard α-helix in *Sa*SbnH (Fig. 2d, and Supplementary Fig. S6).

Not similar to the citryl moiety, the Dae moiety of citryl-Dae does not contribute significant interactions with *Sa*SbnH. The Dae moiety of one of the two citryl-Dae molecules stretched outside of the pocket, mimicking a state before product release. The Dae moiety of the other citryl-Dae molecule was buried in the active site and covalently linked to the cofactor PLP. Tyr373, a residue absolutely conserved among all PLP-dependent amino acid decarboxylases we analyzed (Supplementary Fig. S2), forms the "floor" of the substrate-binding pocket to hold the Dae moiety. Mutation of Tyr373 to alanine reduced the activity of *Sa*SbnH by more than 90% in our decarboxylation assay (Fig. 3).

*Sa*SbnH catalyzes the decarboxylation of the L-configuration Dap moiety of citryl-L-Dap to generate citryl-Dae. A previous study on ODC indicated that the carboxyl group of L-ornithine points to the *re*-side of the PLP, the same side as the PLP-binding lysine, and forms contacts with a phenylalanine [35]. In contrast, DAPDC and the stereo-inverted D-ODC, which both decarboxylate the D-center carboxyl, bind the carboxyl group of the substrate with a pocket at the *si*-side of PLP, the side toward the solvent [36,37]. The carboxyl-contacting phenylalanine of ODC was substituted with a tyrosine in both DAPDC and D-ODC, and the additional oxygen of tyrosine would clash with L-center carboxyl groups and stereoselectively preclude L-configuration substrates [37]. Consistently, a phenylalanine (Phe382) exists at the corresponding position of *Sa*SbnH; thus, it is very likely that Phe382 will contribute to the recognition of the carboxyl group of the L-Dap moiety of citryl-L-Dap. Compared with wild-type *Sa*SbnH, the *Sa*SbnH_F382Y variant lost approximately 60% of the decarboxylation activity. *Sa*SbnH_F382A lost even more activity, which could be due to the change in the electrostatic environment, as with ODC (Fig. 3) [35]. These results support an important role for Phe382 in substrate recognition. Thus, the citryl-L-Dap was unambiguously modeled in the active site based on the citryl-Dae-bound cocrystal structure to further understand the decarboxylation mechanism of *Sa*SbnH (Supplementary Fig. S7).

The proposed decarboxylation mechanism of *Sa*SbnH

Previous mechanistic studies on PLP-dependent amino acid decarboxylases have facilitated the understanding of the decarboxylation mechanism of *Sa*SbnH. In addition to its function on covalently coordinating the cofactor PLP in the resting state, the PLP-bound lysine of ODCs accelerates the formation of external Schiff base with the amino group of ornithine, decarboxylation, and product release [34]. In addition, the conserved cysteine residue in the active site of ODC was also suggested to contribute to Schiff base formation, decarboxylation, and, in particular, carbanion protonation [38]. These two residues are conserved and proposed to play similar catalytic roles in other amino acid decarboxylases, such as DAPDC and ADC [30,36]. In *Sa*SbnH, these two residues are also present at the same positions in the active site. In the modeled complex structure of *Sa*SbnH, the ϵ-amino group of Lys50 is close to the leaving carboxyl group of citryl-L-Dap (Supplementary Fig. S7). Although the thiol group of Cys344 is oriented to the opposite side from the active site in *Sa*SbnH, the corresponding cysteine residue forms multiple conformations and readily forms close contacts with the carboxyl group of the substrates in ODC and DAPDC [27,34,38]. As with ODC, this conserved cysteine might play a role as a general acid to guide correct protonation of the decarboxylated reaction intermediate at Cα [38]. In the decarboxylation experiment, the activities of the K50A and C344A variants of *Sa*SbnH both decreased more than 90% compared with that of the wild-type enzyme. Thus, the structural observations and the mutagenesis analysis both suggested that Lys50 and Cys343 play similar roles in the catalysis of *Sa*SbnH, and the catalytic process is proposed as shown in Fig. 4.

The inhibition of *Sa*SbnH by citrate

The cocrystal structure of *Sa*SbnH in complex with citrate was solved at 1.76 Å resolution. Each of the three *Sa*SbnH molecules in the asymmetric unit bound one citrate molecule at the same site where

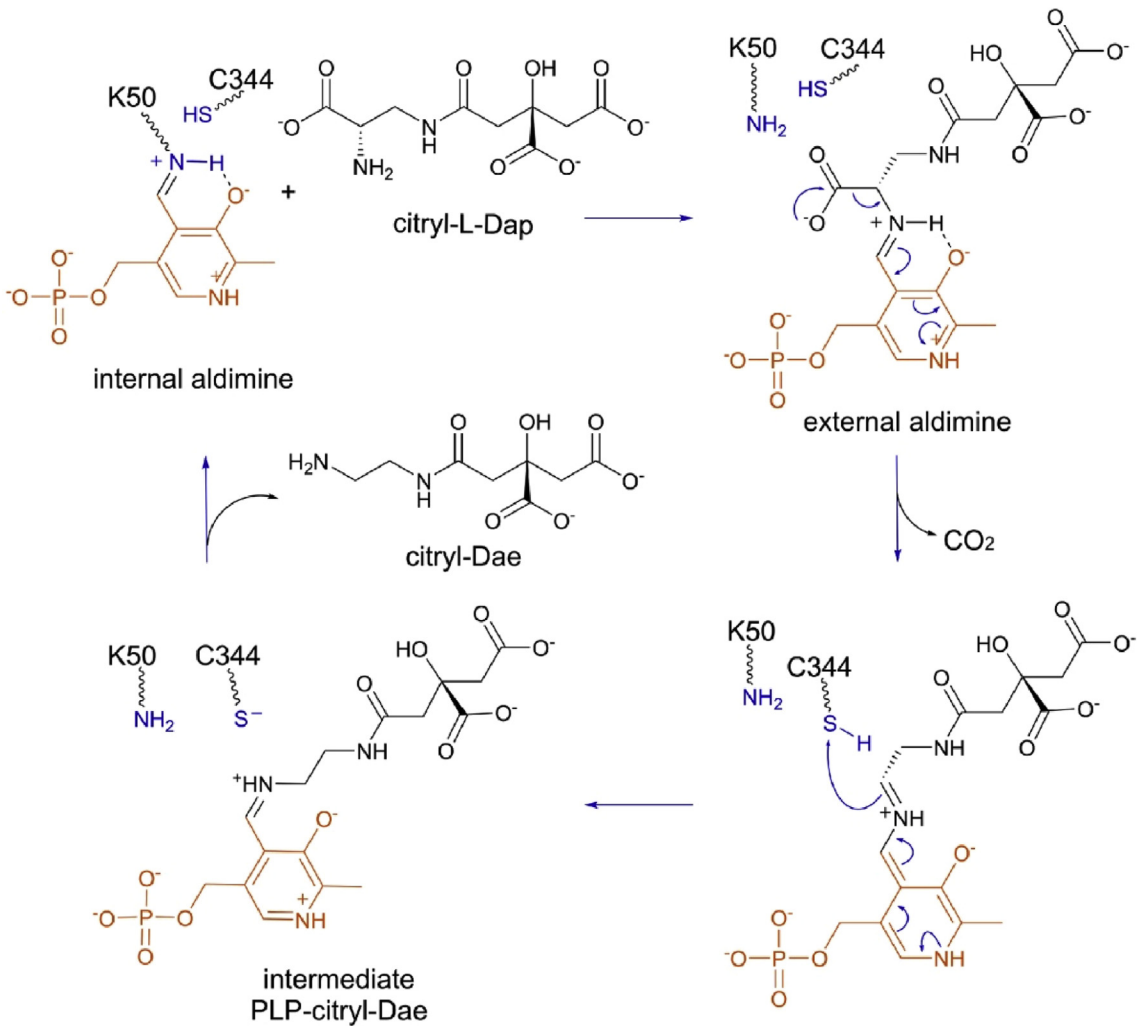

Fig. 4. The proposed decarboxylation process of citryl-L-Dap catalyzed by SbnH. The amino group of Lys50 and the thiol group of Cys344 are important in *Sa*SbnH decarboxylation. These two groups are highlighted in blue. At the resting state, *Sa*SbnH uses the amino group of Lys50 to covalently coordinate the cofactor PLP (orange) via a Schiff-base linkage and forms an internal aldimine. During decarboxylation, PLP changes to form an external aldimine with the amino group of citryl-L-Dap, and then the carboxyl group is cleaved from the Cα carbon of the L-Dap moiety. Then, the thiol group of Cys344 could be used as a "proton donor" to help protonate the carbanion and form the intermediate product PLP-citryl-Dae. Finally, Lys50 forms an internal aldimine with PLP, and citryl-Dae is released.

the citryl group of citryl-Dae binds. However, to our surprise, all three freestanding citrate molecules bound to *Sa*SbnH in a conformation inverse to the citryl group of citryl-Dae (Fig. 5a). Strong positive and negative density appeared when citrate was modeled in the active site according to the conformation of citryl-Dae (Fig. 5b and c). In this inverse conformation, citrate retained all the hydrogen bonding interactions of the citryl group with *Sa*SbnH, and in addition, the two prochiral carbons of citrate formed close hydrophobic contacts with Phe382 (Fig. 5a). In contrast, these hydrophobic contacts did not exist between citryl-Dae and Phe382, and the hydroxyl of the citryl moiety stacked with Phe382 (Fig. 5a). The binding of citrate to *Sa*SbnH was further studied by using fluorescence-based thermal shift assays (TSA). In the presence of 1 mM citrate, the melting temperature (T_m) of wild-type *Sa*SbnH increased by approximately 6.5 °C (Fig. 6a and Supplementary Fig. S8a). Mutations in the citrate-binding residues, such as Arg269, Arg304, Ser308, Trp309, Thr345, Lys347, Tyr373, and Phe382, all significantly reduced the thermal stabilization induced by citrate binding, supporting the specific binding of citrate at the substrate-binding groove of *Sa*SbnH. As controls, the T_m values of other staphyloferrin B synthesis enzymes such as *Sa*SbnE, which uses citrate as a substrate, and *Sa*SbnF, whose substrate also contains a citryl group, were measured and only slightly improved,

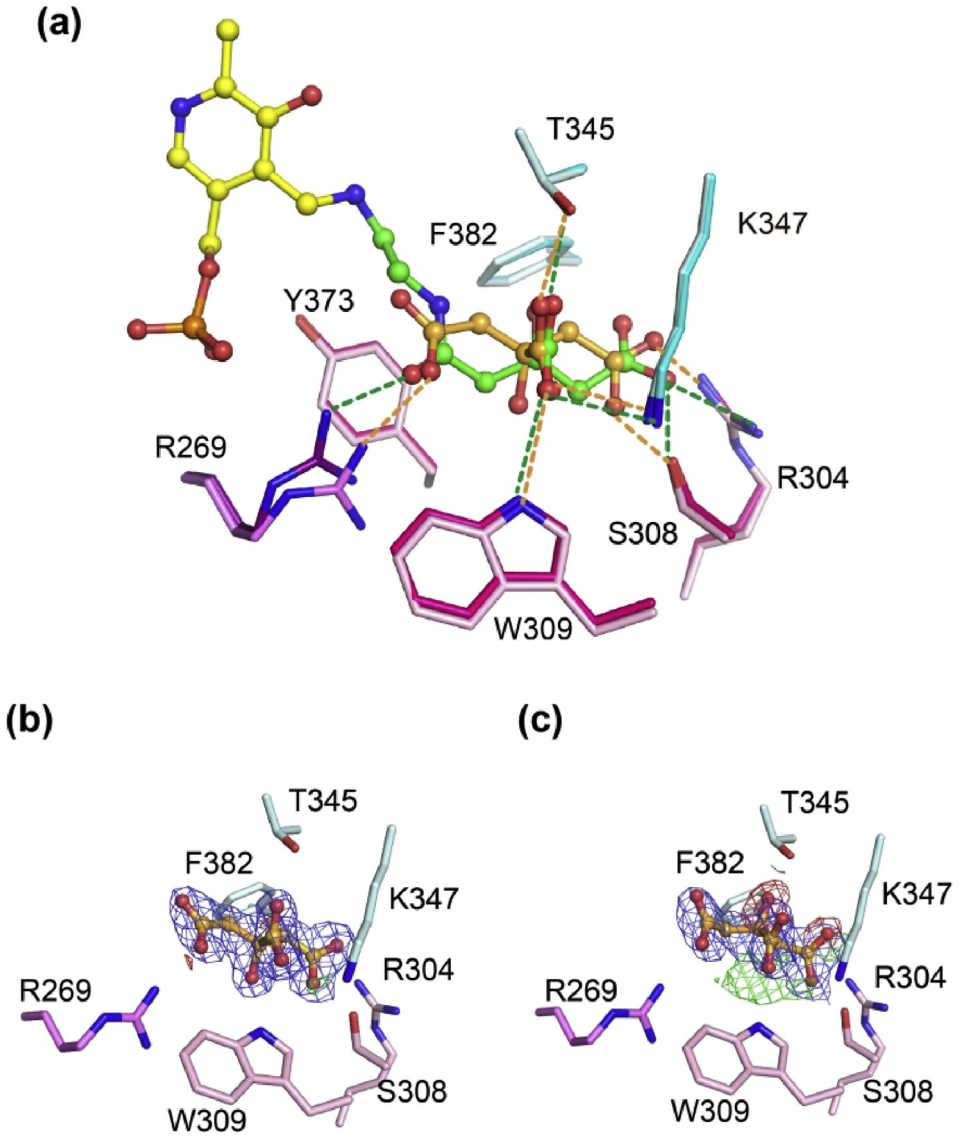

Fig. 5. Citrate binds to *Sa*SbnH in a conformation opposite to that of citryl-Dae. (a) Superposition of the citrate-Dae-bound (colored the same as in Fig. 2a) and citryl-bound (light color) structures revealed the opposite conformations of two compounds bound at the same site of the substrate-binding groove. Hydrogen bonds between *Sa*SbnH and PLP-citryl-Dae are drawn as green dashed lines, and those between *Sa*SbnH and citrate (in orange) are drawn as orange dashed lines. (b, c) The density maps of citrate modeled in two opposite conformations in the groove. The $2F_o-F_c$ composite map (blue) around citrate is contoured at 1.0 σ, and the F_o-F_c difference map (green and red) is contoured at 3.0 σ. Strong negative and positive density appears in the F_o-F_c map if citrate is modeled in the same conformation as citryl-Dae (c).

if at all, by citrate (Fig. 6a and Supplementary Figs. S8b and c), suggesting that the strong binding of citrate is specific to *Sa*SbnH.

Then, the activity of *Sa*SbnH was measured in the presence of various concentrations of citrate by using the *Sa*SbnF-coupled ATP consumption assay. At high concentrations, citrate completely inhibited ATP consumption (Fig. 6b), and the IC_{50} value of citrate was 280 μM (Fig. 6c). Because ATP consumption could be in principle blocked by inhibiting either *Sa*SbnH or *Sa*SbnF, a control assay was performed by incubating *Sa*SbnH with substrate before adding citrate and *Sa*SbnF. ATP consumption was not significantly affected by citrate in the control assay, indicating that citrate indeed inhibited *Sa*SbnH but not *Sa*SbnF, consistent with that citrate specifically bound to *Sa*SbnH but not *Sa*SbnF, as revealed by the previous TSA binding assay. As an important metabolic intermediate of the citric acid cycle (TCA cycle), the physiological concentration of citrate usually reaches 2 mM in normal bacterial cells [39]. Interestingly, the

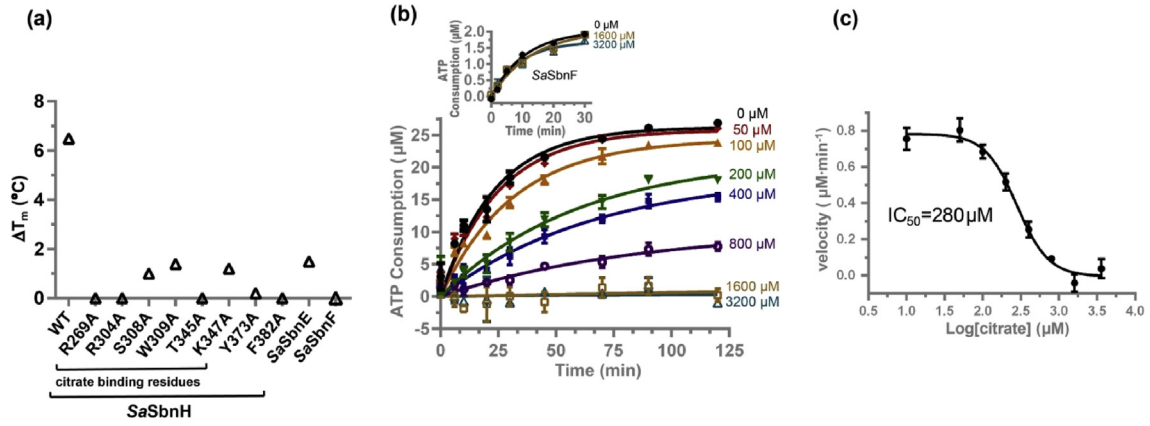

Fig. 6. The inhibition of *Sa*SbnH decarboxylation by citrate. (a) The binding of citrate to *Sa*SbnH and its variants was evaluated by using fluorescence-based thermal shift assays. The melting temperature of wild-type *Sa*SbnH was increased by citrate (1 mM final concentration) at approximately 6.5 °C. The increase in melting temperature became much lower when the citrate-binding residues were mutated in the *Sa*SbnH variants, supporting the specific binding of citrate to the substrate-binding groove of *Sa*SbnH. The small increase in melting temperature of *Sa*SbnE and *Sa*SbnF suggests that citrate binds much weaker (or does not bind) to *Sa*SbnE and *Sa*SbnF than *Sa*SbnH. (b) The activity of *Sa*SbnH in the presence of various concentrations of citrate was measured by using a *Sa*SbnF-coupled reaction. ATP consumption was completely inhibited by citrate at high concentrations. The inset shows a control assay which confirmed that the inhibition of ATP consumption by citrate was not through blocking *Sa*SbnF. (c) The IC_{50} value of citrate was determined to be 280 μM by using the decarboxylation velocities in the presence of various concentrations of citrate.

synthesis of citrate in *S. aureus* is notably down-regulated in iron-restricted conditions [40]. Thus, citrate might serve as a new regulatory factor of staphyloferrin B biosynthesis in response to the environmental iron concentration.

Discussion

We report here the first structure of *Sa*SbnH and its complexes with the intermediate product citryl-Dae, cofactor PLP, and the endogenous inhibitor citrate. This is also the first structural study of the enzymes involved in the assembly of the siderophore staphyloferrin B. Through sequence analysis of the biosynthetic gene clusters in bacterial genomes, several decarboxylase homologs of *Sa*SbnH that synthesize other siderophores, such as butirosin and achromobactin, have been identified. Although the *Sa*SbnH-mediated decarboxylation step is indispensable for staphyloferrin B synthesis [17], in the biosynthesis of the *Pseudomonas syringae* siderophore achromobactin, the decarboxylation step mediated by the *Sa*SbnH homolog can be bypassed by using alternative decarboxylated precursors [41,42]. However, *Sa*SbnH and its homologs involved in siderophore biosynthesis always decarboxylate after the precursors are assembled rather than before they assembled [41,43]. Thus, *Sa*SbnH may represent a unique group of decarboxylases that are different from amino acid decarboxylases, which specifically evolved for siderophore biosynthesis.

The overall structure of *Sa*SbnH is similar to those of other PLP-dependent amino acid decarboxylases, such as ODC, DAPDC, LDC, and ADC [27–30], and the substrate-binding pocket of *Sa*SbnH showed some unique features different from these homologs. Most notably, the citryl group of citryl-L-Dap is not extended toward the specific element, a 3_{10}-helix in the active site, as the substrates of these amino acid decarboxylases did. Instead, the citryl group of citryl-L-Dap is inserted into the dimeric interface of two *Sa*SbnH monomers, forming a more extensive hydrogen-bonding interaction network (Fig. 2a, b, d). However, in this binding mode, the citryl group is close to Phe382, which is the important stereoselective residue conserved in decarboxylases with L-amino acid substrates (Fig. 2d) [28,29,44]. This phenylalanine residue is changed to a tyrosine in the PLP-dependent decarboxylases with D-configuration amino acid substrates, such as DAPDC and D-ODC (Fig. 2d) [27–30,37]. Although the citryl group might prefer to form an additional hydrogen interaction with the hydroxyl group of tyrosine, phenylalanine was finally chosen in evolution to accommodate the L-configuration carboxyl of citryl-L-Dap. Interestingly, by forming additional hydrophobic stacks, Phe382 directed the free-standing citrate molecule to the active site of *Sa*SbnH in the conformation inversed to the citryl group of citryl-L-Dap. The results of TSA and enzymatic experiments both indicated that citrate could specifically bind to the active site and efficiently inhibit the catalysis of *Sa*SbnH.

Considering the high concentration of citrate in bacterial cells [39], citrate could serve as an efficient endogenous inhibitor of *Sa*SbnH.

To compete with the host "nutritional immunity" system for iron acquisition, *S. aureus* produces at least two α-hydroxycarboxylate siderophores named staphyloferrin A and staphyloferrin B. Among them, staphyloferrin A is more similar to a housekeeping iron captor conducive to commensalistic colonization, and staphyloferrin B is believed to play a major role in invasive infection [11]. The staphyloferrin A and B biosynthetic loci are both iron-regulated through Fur binding [10,15]. In addition, recent studies indicated that SbnI, a bifunctional protein encoded by the staphyloferrin B biosynthetic locus, could heme-responsively regulate the transcription of this locus itself [14]. Although both staphyloferrin A and B use citrate as a building block in their biosynthesis, citrate was also reported to play a role in the differential expression of these two siderophores. Under normal conditions, abundant citrate could be synthesized by the TCA cycle citrate synthase and used as a substrate for staphyloferrin A and B biosynthesis [45]. However, iron-restricted conditions induce the iron-sparing response to decrease iron-consuming pathways, including the TCA cycle, which involves many iron-containing enzymes [40,46], and the biosynthesis of staphyloferrin A will be downregulated due to insufficient levels of the substrate citrate [45]. In contrast, the synthesis of staphyloferrin B is not restricted by the TCA cycle activity because its biosynthetic locus encodes a second citrate synthase, SbnG [47]. In this study, citrate was unexpectedly found to efficiently inhibit SbnH with an IC50 value of approximately 280 μM (Fig. 6b, c), a concentration several fold below the physiological concentration of citrate in bacterial cells under normal conditions. Thus, the repression of the biosynthesis of staphyloferrin B by citrate in iron-abundant conditions is very likely. Correspondingly, citrate synthesis in the TCA cycle is significantly downregulated under iron-depleted conditions; thus, the inhibition of SaSbnH by citrate will be removed, and the biosynthesis of staphyloferrin B will be restored for iron acquisition. The regulatory capability of the substrate citrate enriches our understanding of the regulatory mechanism of siderophore biosynthesis (Fig. 7). Interestingly, as a central metabolic pathway in cells, the TCA cycle intermediate products were also observed to regulate other intracellular bioprocesses [48].

In summary, we determined the crystal structure of the key decarboxylase *Sa*SbnH in the biosynthesis of the siderophore staphyloferrin B. *Sa*SbnH showed a typical fold of PLP-dependent dimeric decarboxylase. The key residues involved in substrate recognition and binding of the cofactor PLP were identified by cocrystal structures and further confirmed by site-directed mutagenesis, and the process of PLP-dependent decarboxylation reaction was proposed. In addition, citrate could bind to the active site of *Sa*SbnH with a more favorable conformation and inhibit its catalytic activity. This observation implied a new regulatory mechanism of siderophore biosynthesis in response to iron-regulated TCA cycle activity. Thus, this study provided important new knowledge about the structure, function, and regulation of *Sa*SbnH, which will be helpful for further understanding the process of staphyloferrin B biosynthesis and for designing related inhibitors.

Materials and Methods

Protein expression and purification

The ORF of *Sa*SbnH (UniProtKB: A0A0H3JPF2) was amplified from *S. aureus* (MRSA R3708) genomic DNA by polymerase chain reaction (PCR) and then subcloned into the pET20b vector (Novagen) using the homologous recombination method. A DNA sequence encoding a hexahistidine tag was added at the C-terminus of *Sa*SbnH. The plasmid was transformed into *Escherichia coli* BL21(DE3) (Novagen). *E. coli* cells were cultured in LB medium at 37 °C until the OD_{600} reached ~0.8; then, isopropyl β-D-thiogalactopyranoside (IPTG) was added at a concentration of 150 μM. *E. coli* cells were further cultured overnight at 20 °C to allow the overexpression of the *Sa*SbnH protein before harvesting through centrifugation. *E. coli* cells were resuspended in lysis buffer (500 mM NaCl, 20 mM Tris pH 8.0, 20 mM imidazole) and lysed by sonication. Cell debris was removed by centrifugation at 40,000 *g* for 30 min at 4 °C, and the supernatant was loaded onto a 5-mL Ni-NTA column (Qiagen) preequilibrated with lysis buffer. The column was washed with 50 mL of lysis buffer to remove the contaminants, and then His-tagged *Sa*SbnH was eluted using elution buffer (500 mM NaCl, 20 mM Tris pH 8.0, 100 mM imidazole). The *Sa*SbnH protein was exchanged into gel filtration buffer (200 mM NaCl, 20 mM Tris pH 8.0, 5 mM β-mercaptoethanol), concentrated and loaded onto a HiLoad 16/60 Superdex 200 pg column (GE Healthcare). The fractions containing the *Sa*SbnH protein were buffer exchanged into a final storage buffer (50 mM NaCl, 2 mM Tris pH 8.0), concentrated to 75 mg/mL, and stored at −80 °C before use. The protein purity was above 95% as assessed by SDS-PAGE.

Site-directed mutagenesis of *Sa*SbnH (K50A, R269A, R304A, S308A, W309A, C344A, T345A, K347A, Y373A, F382A, F382Y) was performed by using mutation primer pairs (Supplementary Table S2) to amplify the full-length plasmid via inverse PCR. DpnI was added to remove the parent plasmid template, and then the PCR products were transferred into bacteria. The plasmids of the *Sa*SbnH variants were then isolated, and the mutations were verified by DNA sequencing. The *Sa*SbnH variants were expressed and purified similarly to wild-type *Sa*SbnH.

Crystallography

Crystals of *Sa*SbnH were grown using the sitting drop vapor diffusion method. One microliter of *Sa*SbnH (40 mg/

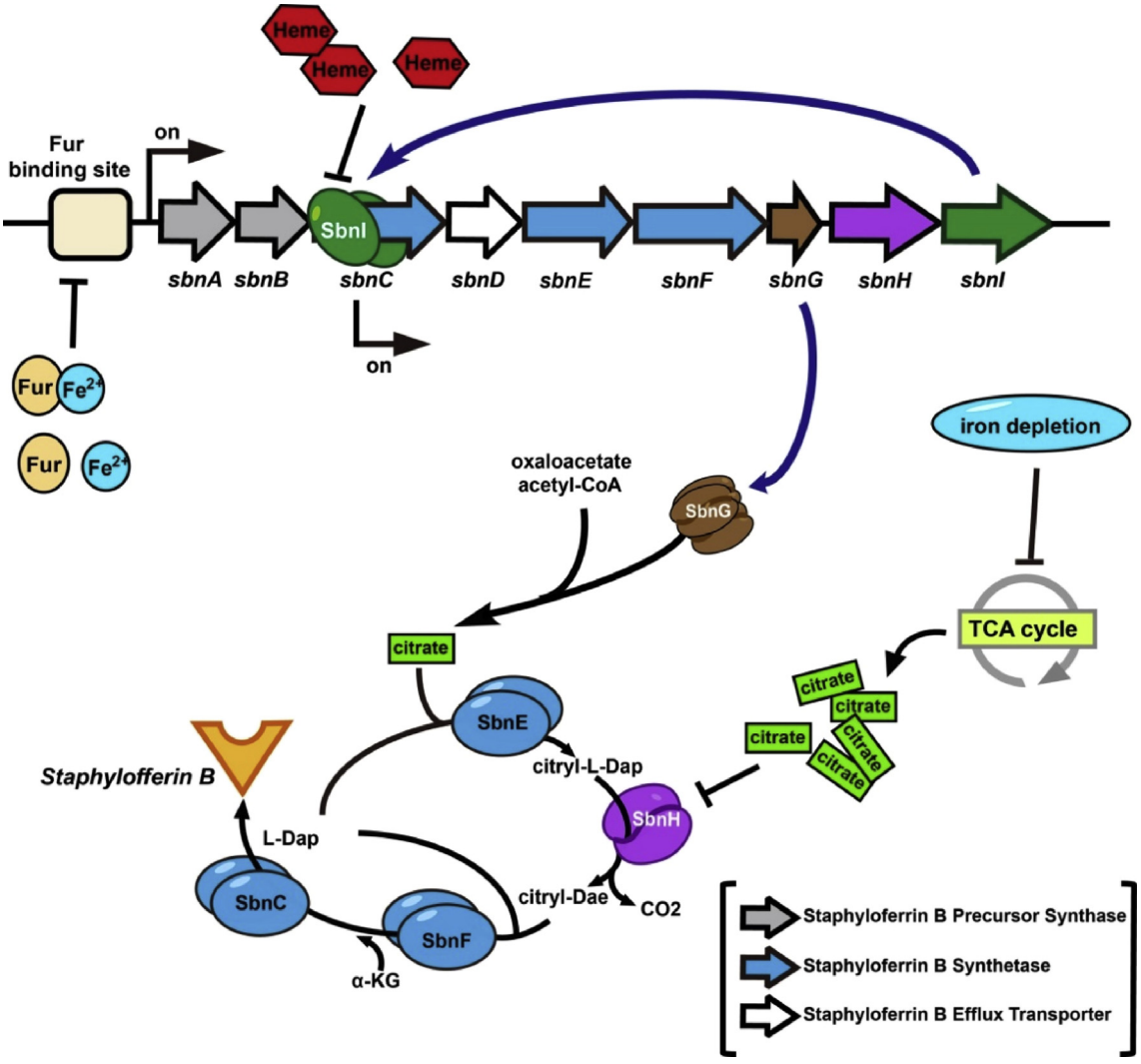

Fig. 7. The regulation mechanisms for the biosynthesis of staphyloferrin B. Different regulation mechanisms interact to regulate the biosynthesis of staphyloferrin B in *Staphylococcus aureus*. Under iron-depleted conditions, the Fur repressor does not bind to DNA, and the *sbn* operon is expressed. SbnI promotes the expression of *sbnD-H* by binding to *sbnC*-coding region. When heme is present, *S. aureus* prefers to use heme as the iron resource, and heme disrupts the DNA-binding of SbnI, blocking the gene expression of *sbnD-H*. In iron-rich conditions, the TCA cycle synthesizes a large amount of citrate, which could downregulate staphyloferrin B biosynthesis by inhibiting the key decarboxylase SbnH.

mL) containing 0.1% agarose was mixed with 1.0 μL of reservoir solution (0.1 M NaAC pH 4.6, 40% PEG 200) and then equilibrated against 70 μL of reservoir solution at 18 °C. High-quality crystals appeared after 3–7 days. Before data collection, crystals were transformed to cryoprotectant solution (the reservoir solution supplemented with 25% glycerol) and flash frozen in liquid nitrogen. The crystals of *Sa*SbnH in complex with citrate were grown using the same method with a reservoir solution containing 0.2 M citrate (0.2 M sodium citrate, 50 mM Bis–Tris pH 6.0, 23% PEG 3350).

To obtain a substrate-bound structure of *Sa*SbnH, the substrate citryl-L-Dap was first biosynthesized *in vitro* by incubating a reaction (10 mL) consisting of 0.4 μM *S. aureus* SbnE (*Sa*SbnE), 10 mM ATP, 5 mM $MgCl_2$, 10 mM sodium citrate, 15 mM L-Dap, and 10 mM HEPES pH 7.5 at room temperature overnight. After removing *Sa*SbnE proteins by using a 10 kDa cut-off centrifugal filter (Millipore), the reaction containing citryl-L-Dap was freeze-dried using a vacuum freeze dryer (alpha 2–4 LD plus, Christ), and the powder was dissolved in 1 mL of 50% PEG 3350. The crystals of *Sa*SbnH_K50A were grown with a reservoir solution of 0.2 M sodium citrate, 50 mM Bis–Tris pH 6.0, and 22% PEG 3350, and then soaked in the citryl-L-Dap solution at 18 °C for 3 h.

The X-ray diffraction data were collected at 100 K at beamlines BL17U1 and BL19U1 at Shanghai Synchrotron Radiation Facility (SSRF) and processed using the HKL2000 [49] and XDS [50] programs. The phase was solved with molecular replacement methods by using the program Molrep [51], and the structure of BtrK (PDB ID: 2J66) was used as the search template. The structure model of *Sa*SbnH

Table 1. Statistics of X-ray diffraction data collection and structure refinement.

	*Sa*SbnH + PLP	*Sa*SbnH + Ciryl-Dae	*Sa*SbnH + citrate
PDB accession codes	6KNI	6KNK	6KNH
Data collection			
Resolution range (Å)	109.32−1.97 (2.08−1.97)[a]	46.74−2.30 (2.35−2.30)	50.00−1.76 (1.82−1.76)
Space group	*C*2	*C*2	*C*2
Cell dimensions			
a, *b*, *c* (Å)	176.6, 80.3, 111.8	176.3, 80.3, 111.5	175.3, 79.6, 111.7
α, β, γ (°)	90.0, 102.2, 90.0	90.0, 102.1, 90.0	90.0, 102.5, 90.0
Unique reflections	105438 (15457)	65898 (4430)	139539 (13626)
Completeness (%)	97.7 (98.6)	97.3 (98.5)	95.1 (93.4)
Mean $I/\sigma I$	9.1 (2.6)	15.1 (2.7)	21.6 (3.5)
Redundancy	3.4 (3.5)	3.3 (3.3)	3.4 (3.3)
R_{merge}[b]	0.10 (0.44)	0.05 (0.37)	0.09 (0.49)
Refinement			
Resolution range (Å)	50.00−1.97	46.76−2.30	50.00−1.76
Reflections for refinement/test	100204/5228	62570/3242	132551/6986
R_{work}[c]/R_{free}[d]	0.20/0.24	0.22/0.24	0.17/0.19
B factors (Å^2)	27.0	41.0	26.0
Nonhydrogen protein atoms	9272	9223	9175
Nonhydrogen ligand atoms	45	57	54
Water oxygen atoms	500	274	464
RMSD bond (Å)	0.008	0.006	0.007
RMSD angle (°)	1.2	1.1	1.2
Ramachandran plot (%)			
Favored	97.7	96.7	97.5
Allowed	2.3	3.3	2.4
Outliers	0	0	0.1

[a] Values in parentheses are for the highest resolution shell.
[b] $R_{merge} = \Sigma_h\Sigma_i|I(h)_i - \langle I(h)\rangle|/\Sigma_h\Sigma_i I(h)_i$, where $I(h)_i$ is the observation of the reflection h and $\langle I(h)\rangle$ is the weighted average intensity for all observations *I* of reflection h.
[c] $R_{work} = \Sigma h||F_{obs}(h)| - |F_{cal}(h)||/\Sigma_h|F_{obs}(h)|$, where $F_{obs}(h)$ and $F_{cal}(h)$ are the observed and calculated structure factors for reflection h, respectively.
[d] R_{free} was calculated as R_{work} using 5% of the reflections which were selected randomly and omitted from refinement.

was refined using COOT [52] and refmac5 [53]. For the complex structure, the small molecule ligands were added manually at the late stage of the refinement. The stereochemistry qualities of the final models were validated using MolProbity [54]. The statistics of data collection and structure refinement are listed in Table 1.

Thermal shift assay

The binding of citrate to the *Sa*SbnH variants was detected using fluorescence-based thermal shift assays (TSAs). The assays were performed in 20 μL reaction volumes in 96-well PCR plates (Life Technologies), and each reaction consisted of a *Sa*SbnH variant (0.4 mg/mL), 4× SYPRO orange fluorescence dye (Sigma-Aldrich), 150 mM NaCl, 100 mM HEPES pH 7.0, 5 μM PLP, and 1 mM citrate. The sample plates were incubated in a StepOnePlus Real-Time PCR system (Life Technologies) at 25 °C for 10 min and then heated from 25 °C to 95 °C at a rate of 1 °C/min. The melting curves were generated by detecting the SYPRO orange fluorescence as a function of temperature. Triplicate assays were applied to all reactions, and the average curves were used for analysis. The protein melting temperature ($T_{m\text{-citrate}}$) values were calculated from the minima of the derivative reporter plots using the built-in StepOne™ software v2.3. The reactions without citrate were used as blank controls ($T_{m\text{-apo}}$). The thermostabilization of each *Sa*SbnH variant upon citrate binding was defined as $\Delta T_m = T_{m\text{-citrate}} - T_{m\text{-apo}}$. The ΔT_m of *Sa*SbnE and *Sa*SbnF by citrate were also measured using the same method.

Enzyme activity of *Sa*SbnH and its variants

A *Sa*SbnF-coupled continuous enzyme assay was used to measure the activity of *Sa*SbnH and its variants. *Sa*SbnF specifically added one L-Dap molecule to each citryl-Dae, the decarboxylation product of *Sa*SbnH, to synthesize the intermediate product Dap-citryl-Dae, and one ATP molecule is hydrolyzed by *Sa*SbnF in this process. The consumption of ATP was detected by using the Ultra-Glo™ Luciferase assay (Promega) following the instructions. First, a 10-mL reaction consisting of 10 μg/mL *Sa*SbnE, 1 mM L-DAP, 100 μM citrate, 100 μM ATP, 40 μg/mL inorganic pyrophosphatase, 50 mM HEPES, pH 7.5, and 0.25 mM $MgCl_2$ was incubated at room temperature for 3 h to biosynthesize the substrate for *Sa*SbnH. Then, the mixture was heated at 100 °C for approximately 10 min to inactivate *Sa*SbnE and inorganic pyrophosphatase. Then, 95.8 μL of the above mixture was added to each tube. The reactions were started by adding 10 μg/mL *Sa*SbnH or its variants, 20 μg/mL *Sa*SbnF, 20 μM ATP, and 10 μM PLP, and the final reaction volume was adjusted to 100 μL. The reactions were carried out at room temperature for 30 min, and then 5 μL of each reaction was transferred to white 384-well plates (Greiner). A total of 5 μL of Kinase-Glo reagent was added to each well to stop the

reactions, and the luminescence was measured after 10 min using a FlexStation 3 multimode microplate reader (Molecular Devices). The reaction without *Sa*SbnH was used as a blank control. A total of 5 μL of an ATP solution at various concentrations (0, 0.98, 1.95, 3.91, 7.81, 15.63, 31.25, 62.5, 125 μM) was mixed with 5 μL of Kinase-Glo reagent, and the luminescence was measured after 10 min to build a standard curve for ATP concentration (Supplementary Fig. S9). Assays were performed in triplicate for all reactions, and the error bar is the SD.

The inhibition of *Sa*SbnH by citrate

To evaluate the inhibitory effect of citrate on *Sa*SbnH, the activities of wild-type *Sa*SbnH in the presence of various concentrations of citrate sodium pH 7.0 (0, 50, 100, 200, 400, 800, 1600, 3200 μM) were measured using the above method. Slightly differently, 5 μL of each 100 μL reaction was transferred to the white 384-well plates (Greiner) at 0, 5, 10, 20, 30, 45, 70, 90, 120 min, and mixed with 5 μL of Kinase-Glo reagent for luminescence measurement. The reaction without *Sa*SbnH was used as the baseline and subtracted when the ATP consumption was calculated. Assays were performed in triplicate for all reactions, and the error bar is the SD.

Blocking either *Sa*SbnH or *Sa*SbnF could, in principle, equally result in the inhibition of ATP consumption. To exclude the possibility that citrate inhibits *Sa*SbnF instead of *Sa*SbnH, a control assay was performed by adding citrate after the reaction of *Sa*SbnH but before the addition of *Sa*SbnF. The ATP consumption of the control assay was measured with the same method. No inhibition by citrate for the control assay confirmed that citrate did not inhibit *Sa*SbnF.

The IC_{50} of citrate against *Sa*SbnH was calculated based on the reaction velocities of *Sa*SbnH at various concentrations of citrate. The reaction velocities (in the first 30 min) were calculated as the slopes by linearly fitting the ATP consumption *vs* the reaction time (at 0, 5, 10, 20, 30 min). The curve of velocity *vs* citrate concentration was then fitted by using a dose-response (inhibition) function in GraphPad Prism 5.

Modeling of citryl-L-Dap into the *Sa*SbnH active site

The crystal structure of *Sa*SbnH in complex with PLP-citryl-Dae was used as a template to model the skeleton of the PLP-citryl-L-Dap molecule into the active site of *Sa*SbnH. Then, the carboxyl group of citryl-L-Dap was put at the *re*-side of PLP to form contacts with Phe382, as observed in ODC and other PLP-dependent amino acid decarboxylases with L-configuration substrates. The structural model was then energy minimized using the MMFF94x force field in Molecular Operating Environment (MOE) software (http://www.chemcomp.com).

Bioinformatics analysis

Structural homologs of *Sa*SbnH were identified using DALI server [26]. Multiple sequence alignments were generated using CLUSTAW program at GenomeNet [55]. The protein structure illustrations were prepared using program PyMOL (www.pymol.org).

Accession number

The coordinates and structure factors of *Sa*SbnH have been deposited in the Protein Data Bank (PDB) under the accession codes 6KNI (with PLP), 6KNH (with citrate), and 6KNK (with citryl-Dae).

Acknowledgments

The authors thank the staff of beamlines BL17U1 and BL19U1 at Shanghai Synchrotron Radiation Facility, Shanghai, People's Republic of China, for assistance during data collection. This research was supported by National Key Research and Development Program (No. 2017YFE0109900), National Natural Science Foundation of China (No. 81773636, 81803435), Guangdong Natural Science Foundation (No. 2017A030313123), Program for Guangdong Introducing Innovative and Entrepreneurial Teams (No. 2016ZT06Y337), Opening Project of Guangdong Province Key Laboratory of Computational Science at the Sun Yat-sen University (No. 2018019), and Guangdong Provincial Key Laboratory of Chiral Molecule and Drug Discovery (2019B030301005).

Author Contributions

J.T. and Y.J. designed and performed experiments. Q.G. and J.X. contributed to data analysis. H.Z. supervised the research. J.T. and H.Z. wrote the manuscript. All authors approved the final version of the manuscript.

Declaration of Interest

None.

Appendix A. Supplementary data

Supplementary data to this article can be found online at https://doi.org/10.1016/j.jmb.2019.10.009.

Received 15 August 2019;
Received in revised form 8 October 2019;
Accepted 10 October 2019
Available online 18 October 2019

Keywords:
Crystal structure;
Citrate;
Endogenous inhibitor;
Staphylococcus aureus;
PLP-dependent decarboxylase

† Both authors contributed equally to this work.

References

[1] C. Ratledge, L.G. Dover, Iron metabolism in pathogenic bacteria, Annu. Rev. Microbiol. 54 (2000) 881–941.

[2] B.R. Wilson, A.R. Bogdan, M. Miyazawa, K. Hashimoto, Y. Tsuji, Siderophores in iron metabolism: from mechanism to therapy potential, Trends Mol. Med. 22 (2016) 1077–1090.

[3] O. Lewinson, N. Livnat-Levanon, Mechanism of action of ABC importers: conservation, divergence, and physiological adaptations, J. Mol. Biol. 429 (2017) 606–619.

[4] M.I. Hood, E.P. Skaar, Nutritional immunity: transition metals at the pathogen-host interface, Nat. Rev. Microbiol. 10 (2012) 525–537.

[5] T.A. Wencewicz, Crossroads of antibiotic resistance and biosynthesis, J. Mol. Biol. (2019). https://doi.org/10.1016/j.jmb.2019.06.033.

[6] W. Neumann, A. Gulati, E.M. Nolan, Metal homeostasis in infectious disease: recent advances in bacterial metallophores and the human metal-withholding response, Curr. Opin. Chem. Biol. 37 (2017) 10–18.

[7] F.D. Lowy, Staphylococcus aureus infections, N. Engl. J. Med. 339 (1998) 520–532.

[8] S. Konetschny-Rapp, G. Jung, J. Meiwes, H. Zahner, A. Staphyloferrin, A structurally new siderophore from staphylococci, Eur. J. Biochem. 191 (1990) 65–74.

[9] H. Drechsel, S. Freund, G. Nicholson, H. Haag, O. Jung, H. Zahner, et al., Purification and chemical characterization of staphyloferrin B, a hydrophilic siderophore from staphylococci, Biometals 6 (1993) 185–192.

[10] F.C. Beasley, E.D. Vines, J.C. Grigg, Q. Zheng, S. Liu, G.A. Lajoie, et al., Characterization of staphyloferrin A biosynthetic and transport mutants in Staphylococcus aureus, Mol. Microbiol. 72 (2009) 947–963.

[11] J.R. Sheldon, D.E. Heinrichs, Recent developments in understanding the iron acquisition strategies of gram positive pathogens, FEMS Microbiol. Rev. 39 (2015) 592–630.

[12] F. Hanses, C. Roux, P.M. Dunman, B. Salzberger, J.C. Lee, Staphylococcus aureus gene expression in a rat model of infective endocarditis, Genome Med. 6 (2014) 93.

[13] Y. Xu, R.G. Maltesen, L.H. Larsen, H.C. Schonheyder, V.Q. Le, J.L. Nielsen, et al., In vivo gene expression in a Staphylococcus aureus prosthetic joint infection characterized by RNA sequencing and metabolomics: a pilot study, BMC Microbiol. 16 (2016) 80.

[14] H.A. Laakso, C.L. Marolda, T.B. Pinter, M.J. Stillman, D.E. Heinrichs, A heme-responsive regulator controls synthesis of staphyloferrin B in Staphylococcus aureus, J. Biol. Chem. 291 (2016) 29–40.

[15] S.E. Dale, A. Doherty-Kirby, G. Lajoie, D.E. Heinrichs, Role of siderophore biosynthesis in virulence of Staphylococcus aureus: identification and characterization of genes involved in production of a siderophore, Infect. Immun. 72 (2004) 29–37.

[16] A. Tripathi, M.M. Schofield, G.E. Chlipala, P.J. Schultz, I. Yim, S.A. Newmister, et al., Baulamycins A and B, broad-spectrum antibiotics identified as inhibitors of siderophore biosynthesis in Staphylococcus aureus and Bacillus anthracis, J. Am. Chem. Soc. 136 (2014) 1579–1586.

[17] J. Cheung, F.C. Beasley, S. Liu, G.A. Lajoie, D.E. Heinrichs, Molecular characterization of staphyloferrin B biosynthesis in Staphylococcus aureus, Mol. Microbiol. 74 (2009) 594–608.

[18] E. Sandmeier, T.I. Hale, P. Christen, Multiple evolutionary origin of pyridoxal-5′-phosphate-dependent amino acid decarboxylases, Eur. J. Biochem. 221 (1994) 997–1002.

[19] J.N. Jansonius, Structure, evolution and action of vitamin B6-dependent enzymes, Curr. Opin. Struct. Biol. 8 (1998) 759–769.

[20] L.J. Marton, A.E. Pegg, Polyamines as targets for therapeutic intervention, Annu. Rev. Pharmacol. Toxicol. 35 (1995) 55–91.

[21] P. Babokhov, A.O. Sanyaolu, W.A. Oyibo, A.F. Fagbenro-Beyioku, N.C. Iriemenam, A current analysis of chemotherapy strategies for the treatment of human African trypanosomiasis, Pathog. Glob. Health 107 (2013) 242–252.

[22] N. LoGiudice, L. Le, I. Abuan, Y. Leizorek, S.C. Roberts, Alpha-difluoromethylornithine, an irreversible inhibitor of polyamine biosynthesis, as a therapeutic strategy against hyperproliferative and infectious diseases, Med. Sci. 6 (2018) 12.

[23] M.J. Kan, J.E. Lee, J.G. Wilson, A.L. Everhart, C.M. Brown, A.N. Hoofnagle, et al., Arginine deprivation and immune suppression in a mouse model of Alzheimer's disease, J. Neurosci. 35 (2015) 5969–5982.

[24] Y.W. Cheng, C.C. Chang, T.S. Chang, H.H. Li, H.C. Hung, G.Y. Liu, et al., Abeta stimulates microglial activation through antizyme-dependent downregulation of ornithine decarboxylase, J. Cell. Physiol. 234 (2019) 9733–9745.

[25] C.A. Hutton, T.J. Southwood, J.J. Turner, Inhibitors of lysine biosynthesis as antibacterial agents, Mini Rev. Med. Chem. 3 (2003) 115–127.

[26] L. Holm, L.M. Laakso, Dali server update, Nucleic Acids Res. 44 (2016) W351–W355.

[27] S.S. Ray, J.B. Bonanno, K.R. Rajashankar, M.G. Pinho, G. He, H. De Lencastre, et al., Cocrystal structures of diaminopimelate decarboxylase: mechanism, evolution, and inhibition of an antibiotic resistance accessory factor, Structure 10 (2002) 1499–1508.

[28] J. Lee, A.J. Michael, D. Martynowski, E.J. Goldsmith, M.A. Phillips, Phylogenetic diversity and the structural basis of substrate specificity in the beta/alpha-barrel fold basic amino acid decarboxylases, J. Biol. Chem. 282 (2007) 27115–27125.

[29] H.Y. Sagong, H.F. Son, S. Kim, Y.H. Kim, I.K. Kim, K.J. Kim, Crystal structure and pyridoxal 5-phosphate binding Property of lysine decarboxylase from Selenomonas ruminantium, PLoS One 11 (2016) e0166667.

[30] X. Deng, J. Lee, A.J. Michael, D.R. Tomchick, E.J. Goldsmith, M.A. Phillips, Evolution of substrate specificity within a diverse family of beta/alpha-barrel-fold basic amino acid decarboxylases: X-ray structure determination of enzymes with specificity for L-arginine and carboxynorspermidine, J. Biol. Chem. 285 (2010) 25708–25719.

[31] E. Krissinel, K. Henrick, Inference of macromolecular assemblies from crystalline state, J. Mol. Biol. 372 (2007) 774–797.

[32] M.G. Peverelli, da Soares, T.P. Costa, N. Kirby, M.A. Perugini, Dimerization of bacterial diaminopimelate decarboxylase is essential for catalysis, J. Biol. Chem. 291 (2016) 9785–9795.

[33] A.D. Kern, M.A. Oliveira, P. Coffino, M.L. Hackert, Structure of mammalian ornithine decarboxylase at 1.6 A resolution:

stereochemical implications of PLP-dependent amino acid decarboxylases, Structure 7 (1999) 567–581.
[34] A.L. Osterman, H.B. Brooks, L. Jackson, J.J. Abbott, M.A. Phillips, Lysine-69 plays a key role in catalysis by ornithine decarboxylase through acceleration of the Schiff base formation, decarboxylation, and product release steps, Biochemistry 38 (1999) 11814–11826.
[35] L.K. Jackson, H.B. Brooks, D.P. Myers, M.A. Phillips, Ornithine decarboxylase promotes catalysis by binding the carboxylate in a buried pocket containing phenylalanine 397, Biochemistry 42 (2003) 2933–2940.
[36] T. Hu, D. Wu, J. Chen, J. Ding, H. Jiang, X. Shen, The catalytic intermediate stabilized by a "down" active site loop for diaminopimelate decarboxylase from Helicobacter pylori. Enzymatic characterization with crystal structure analysis, J. Biol. Chem. 283 (2008) 21284–21293.
[37] R.S. Phillips, P. Poteh, D. Krajcovic, K.A. Miller, T.R. Hoover, Crystal structure of d-ornithine/d-lysine decarboxylase, a stereoinverting decarboxylase: implications for substrate specificity and stereospecificity of fold III decarboxylases, Biochemistry 58 (2019) 1038–1042.
[38] L.K. Jackson, H.B. Brooks, A.L. Osterman, E.J. Goldsmith, M.A. Phillips, Altering the reaction specificity of eukaryotic ornithine decarboxylase, Biochemistry 39 (2000) 11247–11257.
[39] B.D. Bennett, E.H. Kimball, M. Gao, R. Osterhout, S.J. Van Dien, J.D. Rabinowitz, Absolute metabolite concentrations and implied enzyme active site occupancy in Escherichia coli, Nat. Chem. Biol. 5 (2009) 593–599.
[40] D.B. Friedman, D.L. Stauff, G. Pishchany, C.W. Whitwell, V.J. Torres, E.P. Skaar, Staphylococcus aureus redirects central metabolism to increase iron availability, PLoS Pathog. 2 (2006) e87.
[41] A.D. Berti, M.G. Thomas, Analysis of achromobactin biosynthesis by Pseudomonas syringae pv. syringae B728a, J. Bacteriol. 191 (2009) 4594–4604.
[42] S. Schmelz, C.H. Botting, L. Song, N.F. Kadi, G.L. Challis, J.H. Naismith, Structural basis for acyl acceptor specificity in the achromobactin biosynthetic enzyme AcsD, J. Mol. Biol. 412 (2011) 495–504.
[43] Y. Li, N.M. Llewellyn, R. Giri, F. Huang, J.B. Spencer, Biosynthesis of the unique amino acid side chain of butirosin: possible protective-group chemistry in an acyl carrier protein-mediated pathway, Chem Biol 12 (2005) 665–675.
[44] R. Shah, R. Akella, E.J. Goldsmith, M.A. Phillips, X-ray structure of Paramecium bursaria Chlorella virus arginine decarboxylase: insight into the structural basis for substrate specificity, Biochemistry 46 (2007) 2831–2841.
[45] J.R. Sheldon, C.L. Marolda, D.E. Heinrichs, TCA cycle activity in Staphylococcus aureus is essential for iron-regulated synthesis of staphyloferrin A, but not staphyloferrin B: the benefit of a second citrate synthase, Mol. Microbiol. 92 (2014) 824–839.
[46] G.T. Smaldone, O. Revelles, A. Gaballa, U. Sauer, H. Antelmann, J.D. Helmann, A global investigation of the Bacillus subtilis iron-sparing response identifies major changes in metabolism, J. Bacteriol. 194 (2012) 2594–2605.
[47] M.J. Kobylarz, J.C. Grigg, J.R. Sheldon, D.E. Heinrichs, M.E. Murphy, SbnG, a citrate synthase in Staphylococcus aureus: a new fold on an old enzyme, J. Biol. Chem. 289 (2014) 33797–33807.
[48] H. Tarhonskaya, R.P. Nowak, C. Johansson, A. Szykowska, A. Tumber, R.L. Hancock, et al., Studies on the interaction of the Histone Demethylase KDM5B with tricarboxylic acid cycle intermediates, J. Mol. Biol. 429 (2017) 2895–2906.
[49] Z. Otwinowski, W. Minor, Processing of X-ray diffraction data collected in oscillation mode, Methods Enzymol. 276 (1997) 307–326.
[50] W. Kabsch, XDS, Acta Crystallogr D Biol Crystallogr. 66 (2010) 125–132.
[51] A. Vagin, A. Teplyakov, Molecular replacement with MOLREP, Acta Crystallogr. D Biol. Crystallogr. 66 (2010) 22–25.
[52] P. Emsley, B. Lohkamp, W.G. Scott, K. Cowtan, Features and development of Coot, Acta Crystallogr. D Biol. Crystallogr. 66 (2010) 486–501.
[53] G.N. Murshudov, P. Skubak, A.A. Lebedev, N.S. Pannu, R.A. Steiner, R.A. Nicholls, et al., REFMAC5 for the refinement of macromolecular crystal structures, Acta Crystallogr. D Biol. Crystallogr. 67 (2011) 355–367.
[54] C.J. Williams, J.J. Headd, N.W. Moriarty, M.G. Prisant, L.L. Videau, L.N. Deis, et al., MolProbity: more and better reference data for improved all-atom structure validation, Protein Sci. 27 (2018) 293–315.
[55] J.D. Thompson, D.G. Higgins, T.J. Gibson, W. CLUSTAL, Improving the sensitivity of progressive multiple sequence alignment through sequence weighting, position-specific gap penalties and weight matrix choice, Nucleic Acids Res. 22 (1994) 4673–4680.